Journal of Geophysical Research: Solid Earth

Supporting Information for

A dipping, thick segment of the Farallon Slab beneath Central US

Daoyuan Sun[1,2]*, Michael Gurnis[3,4], Jason Saleeby[4], Don Helmberger[3,4]

[1]Laboratory of Seismology and Physics of Earth's Interior, School of Earth and Space Sciences, University of Science and Technology of China, Hefei, Anhui 230026, China;
[2]National Geophysics Observatory at Mengcheng, Anhui 233500, China;
[3]Seismological Laboratory, California Institute of Technology, Caltech, Pasadena, CA 91125;
[4]Division of Geological and Planetary Sciences, California Institute of Technology, Pasadena, CA 91125, USA.

Contents of this file

Introduction

The detailed waveform modeling process, resolution tests are discussed here.

Text S1. Multi-path Detector analysis

The Multi-path Detector (MPD) was developed to examine the waveform complexities across a dense seismic array in a more systematical manner [*Sun and Helmberger*, 2011; *Sun et al.*, 2009]. The complexities in the waveforms indicate the multi-pathing effects, including in-plane and out-plane multi-pathing, which are used to map the sharp structures in the deep earth directly. The MPD method simulates each observed body waveform by performing a decomposition with $[S(t) + C \times S(t - \Delta_{LR})]/2$, where S(t) is the synthetic for a reference model and has a simple pulse shape typically. Time separation (Δ_{LR}) and amplitude ratio (C) are determined by obtaining a high cross correlation between a simulated waveform and the data (Fig. 4). The travel time of the composite waveform relative to the reference model synthetic is

then defined as Δ_T, which is similar to travel time measurements in conventional tomography but with higher accuracy (Fig. 4). The Δ_{LR} describes the waveform complexity. Larger values of Δ_{LR} inidicate stronger mutli-pathing and more distorted waveforms. Although more complete simulations can be made by adding diffracted arrivals [*Sun and Helmberger*, 2011], most of the distortions can be tracked with this simple approach. With the maps of Δ_{LR} values, we can easily recognize features with high- or low-velocity anomalies and define their sharp edges.

Sun and Helmberger [2011] developed the MPD patterns for a slab structure and showed that a slab produces early arrivals (small Δ_T values, blue color in the left column of Fig. 5), strong waveform distortion (large Δ_{LR} values, red color in the middle column of Fig. 5). The product of Δ_T and Δ_{LR} enhances the multi-pathing signatures caused by the high velocity anomaly (blue color in the right columns of Fig. 5).

Text S2 Resolution test for seismic modeling

Models included various idealizations constructed from existing tomographic models with the slab extending to different depth (Fig. S7) and slabs with various percentage velocity increase and shapes (Fig. 8 and Fig. S8-S9) are tested. In the upper mantle, we adopt the LLNL P velocity model assuming R = dlnVs/dlnVp = 2.

We have included numerical experiments involving the addition of horizontal layering, including low velocity zones and structures reminiscent of folded slab in studies in fluid dynamic models (i.e. and used in seismic interpretation of the North American seismic anomaly, Fig. S8). The former produces ringing which some observations display while the latter can produce broadening. Given the complexity of those waveforms all of these effects could be involved.

The sharpness of the slab interface affects multi-pathing. Fig. S9 displays synthetics for slab models with gradual boundaries. If the boundary is gradual (~100 km), the waveforms lose their complexity. In order to explain the multi-pathing in the data, we estimate that the transition width should be less than 60 km.

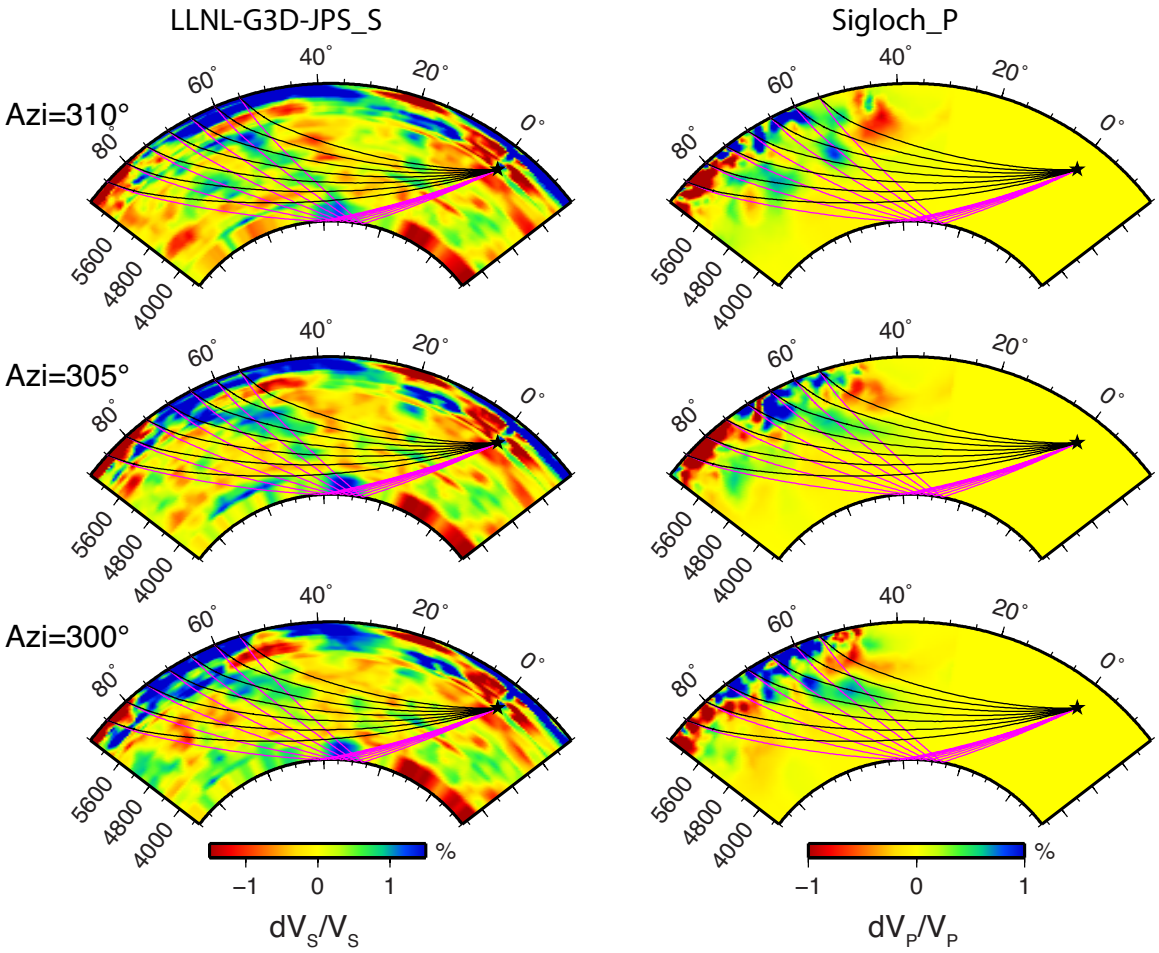

Figure S1. 2D cross sections through two different tomography models. Left column is the LLNL-G3-JPS S-velocity model. Right column is *Sigloch*'s [2011] P-velocity model.

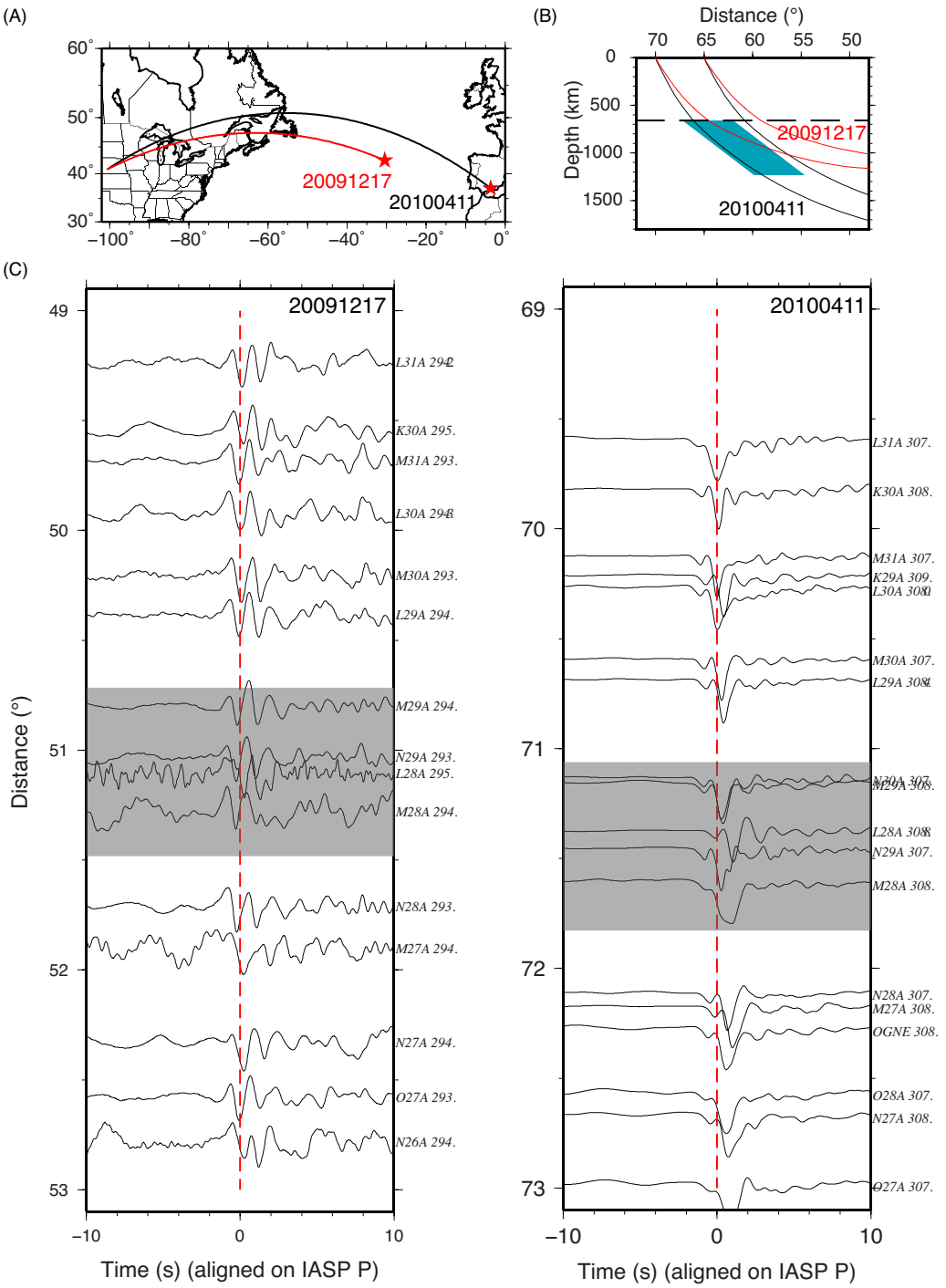

Figure S2. P data examples. (A) displays the event locations of the shallow ridge event (20091217) and the deep Spain event (20100411). The event 20091217 samples the proposed slab at a much shallower angle as displayed in (B). (C) P data for both events. For the same stations in the shadowed region, the deep Spain event has advanced P (N29A) and complicated waveform (M28A). Such variations are not obvious in the records of event 20091217.

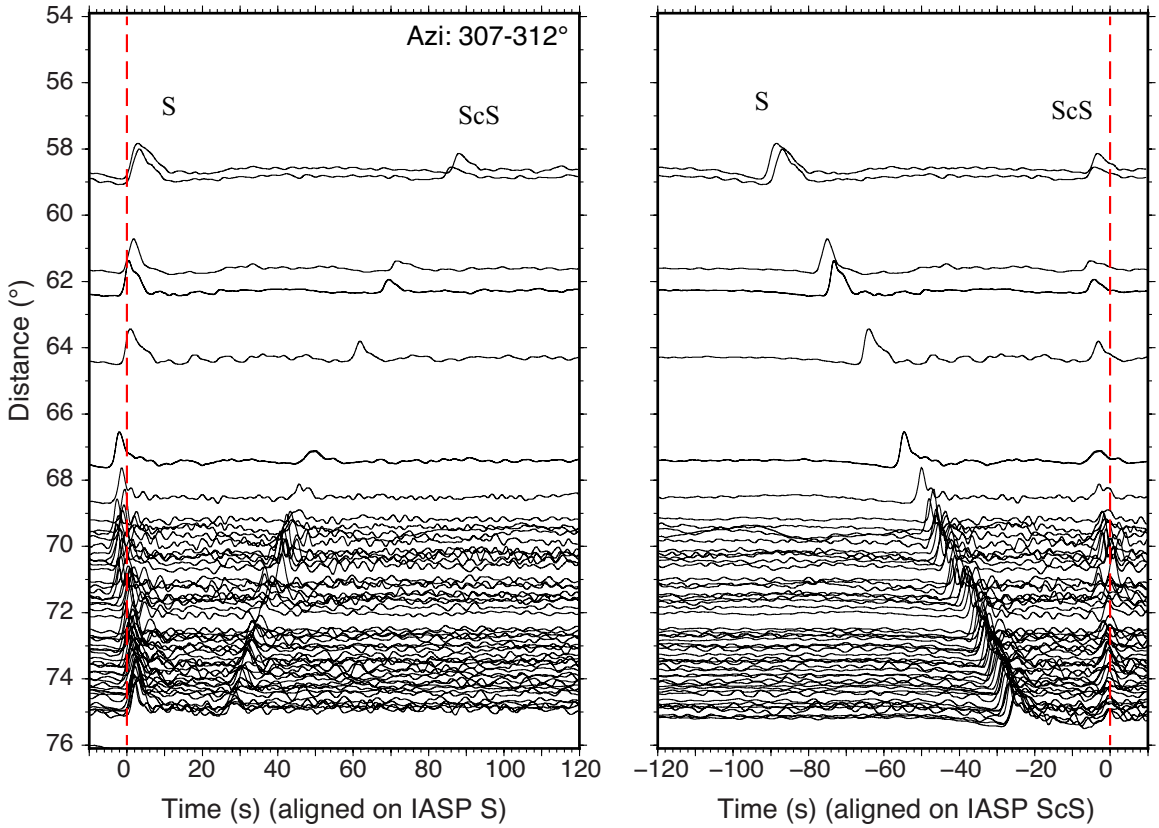

Figure S3. Example of the SH data at the azimuth of 307° to 312°. The data at the left column is aligned on predicted IASP S arrivals with ScS on the right. S arrivals arrive earlier in the distance range of 66° and 70° indicating sampling a fast anomaly. In contrast, the ScS arrivals do not have such variation in travel times as displayed in the right column.

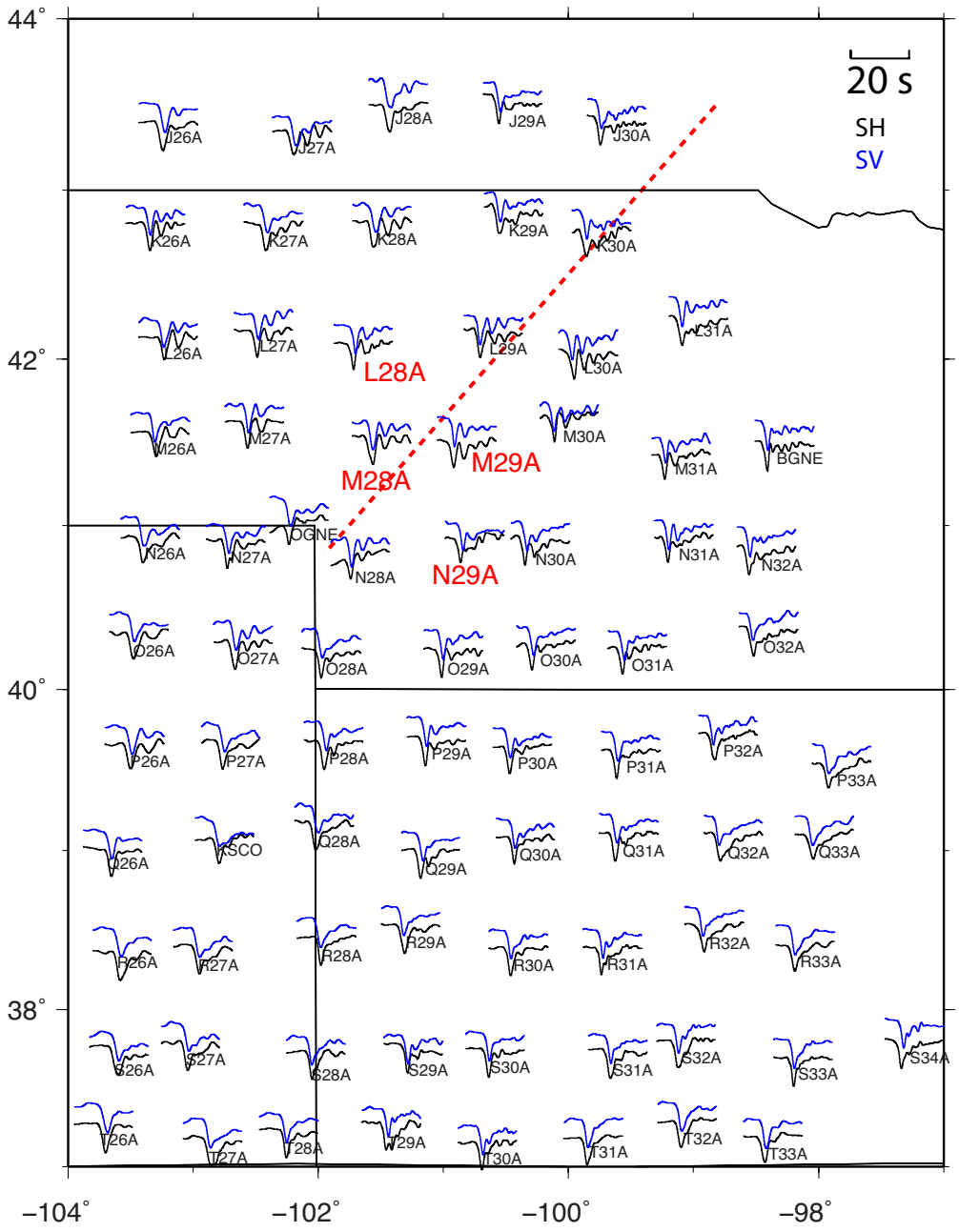

Figure S4. Comparison between the SH (black) and SV (blue) data. The station name is listed below every trace. The red dash line indicates sharp edge with strong azimuthal multi-pathing occurs.

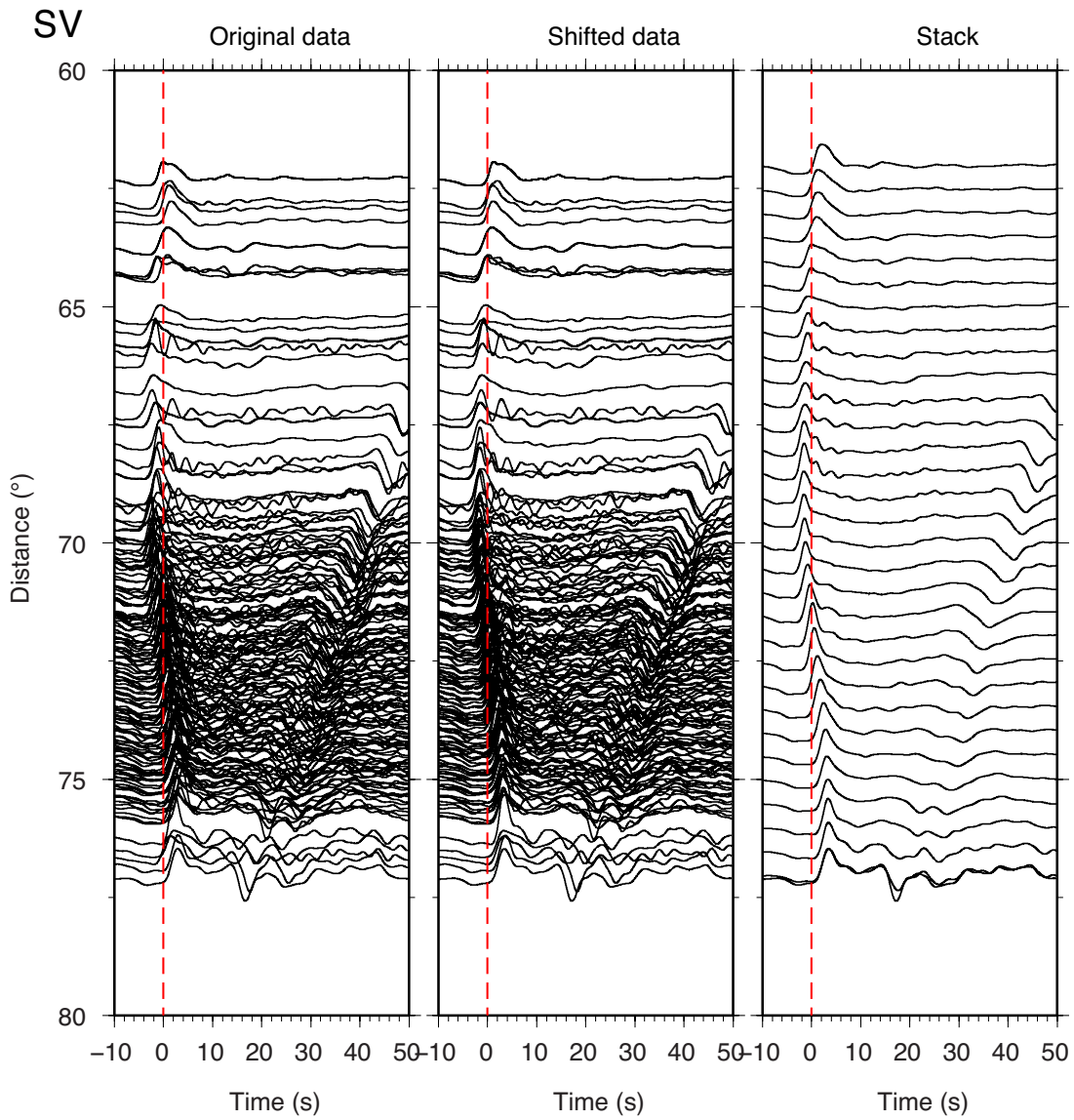

Figure S5. An example section of the SV data following the procedure given in Fig. 6B.

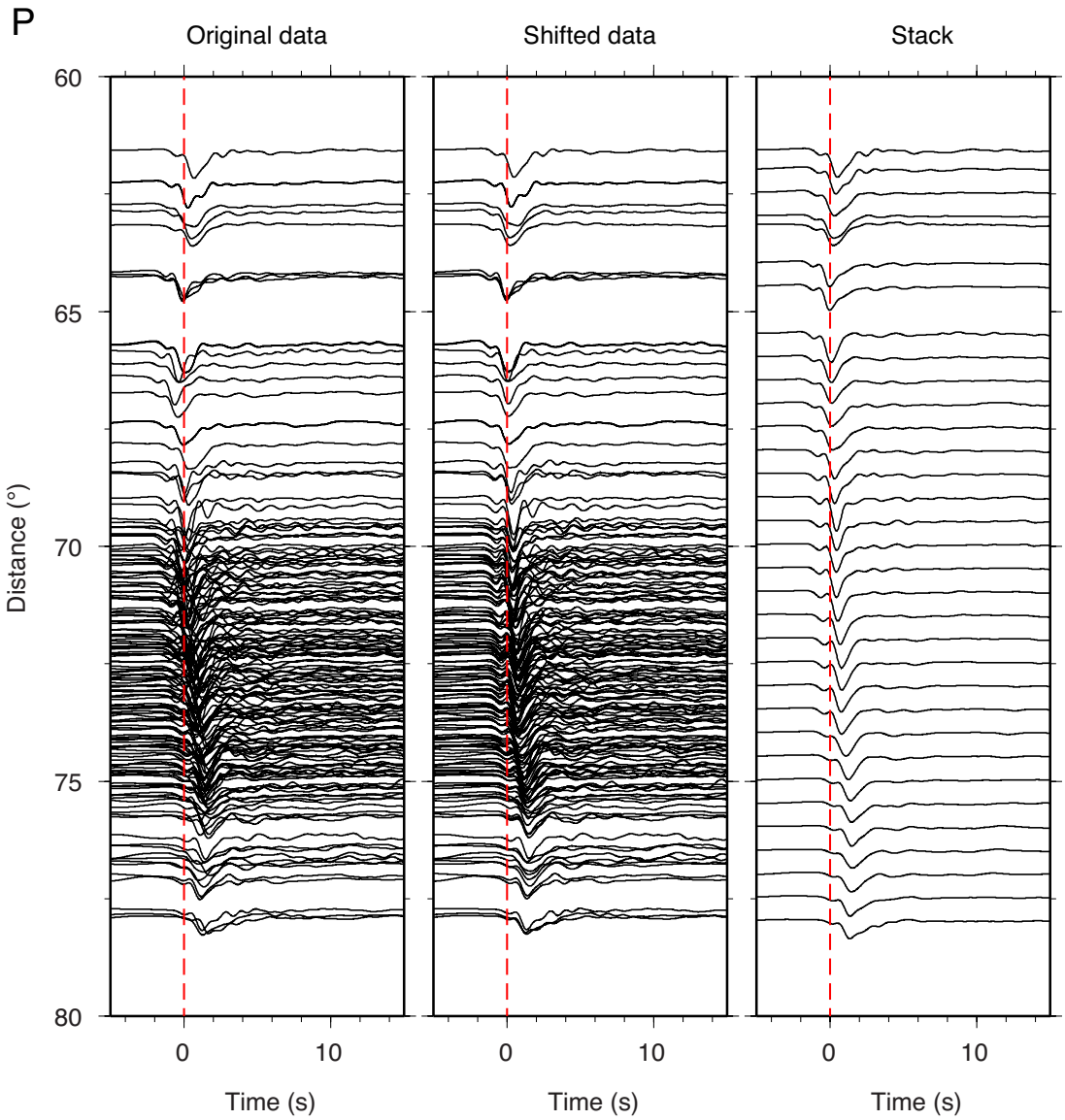

Figure S6. Presentation of the P waveform data analysis.

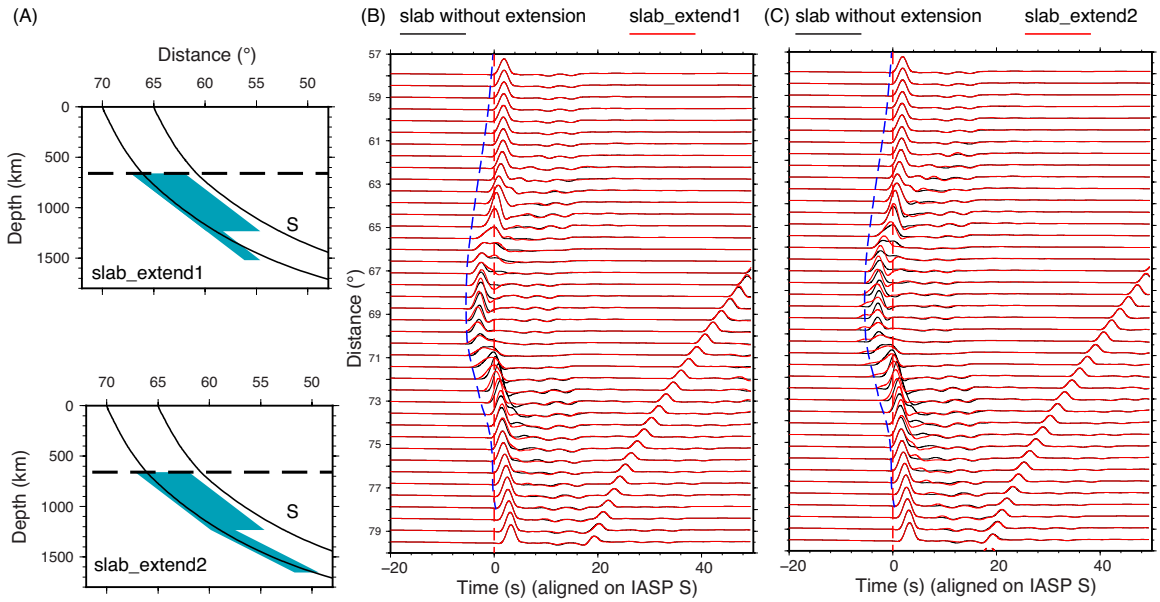

Figure S7. Predicted SH from (A) two models with high velocity slab structures extending deeper. The extension part in the top model has the same dipping angle. In the bottom model, the extension part varies the dipping angle by following the ray paths. Their synthetics are displayed as the red traces in (B) and (C). The black traces are synthetics for slab without the extension part.

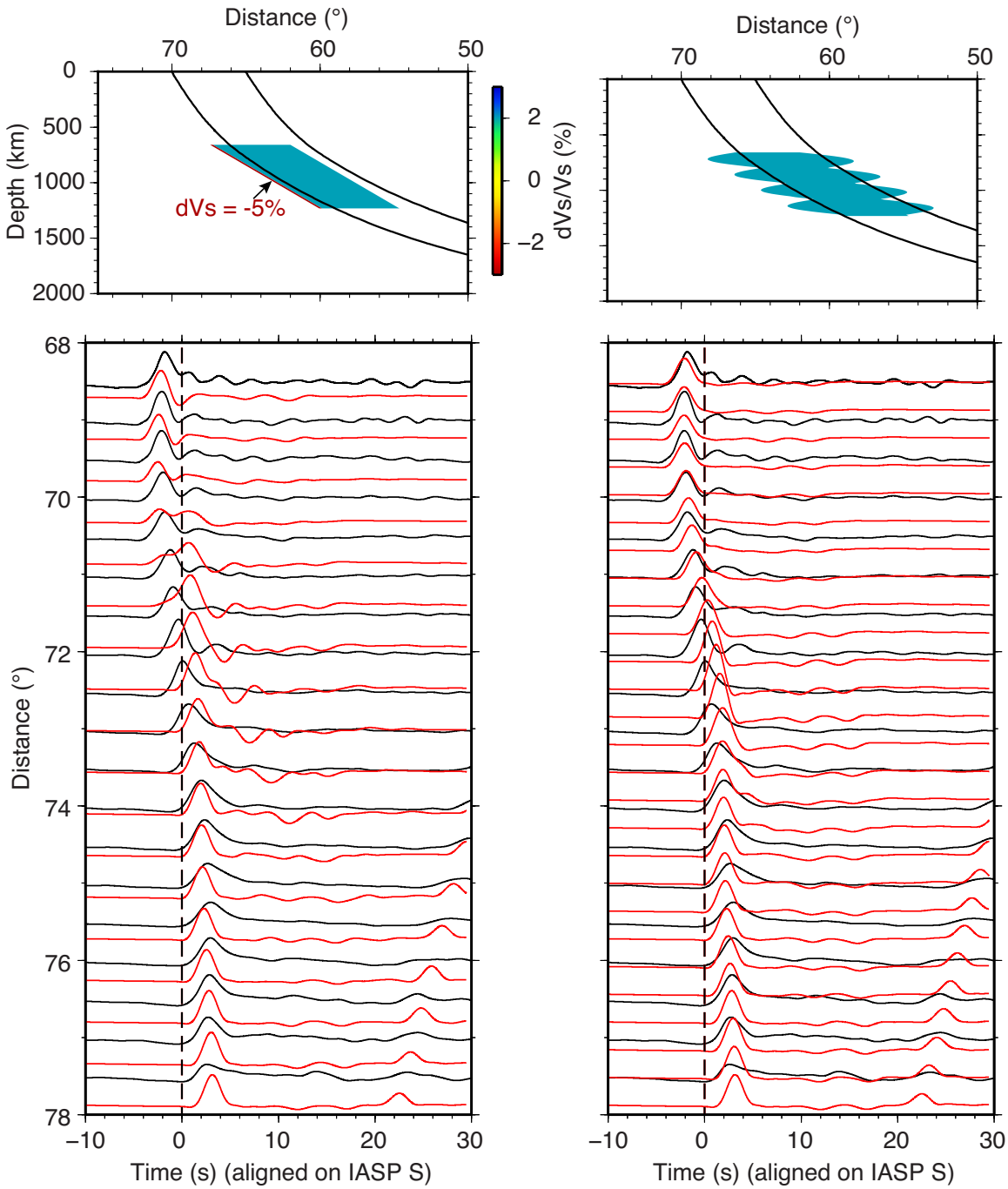

Figure S8. Predicted SH for (left) a slab model with a thin low velocity layer attached to the slab surface and (right) a buckled slab model (red). The black traces are the synthetics for the simple slab model (left column in Fig. 8).

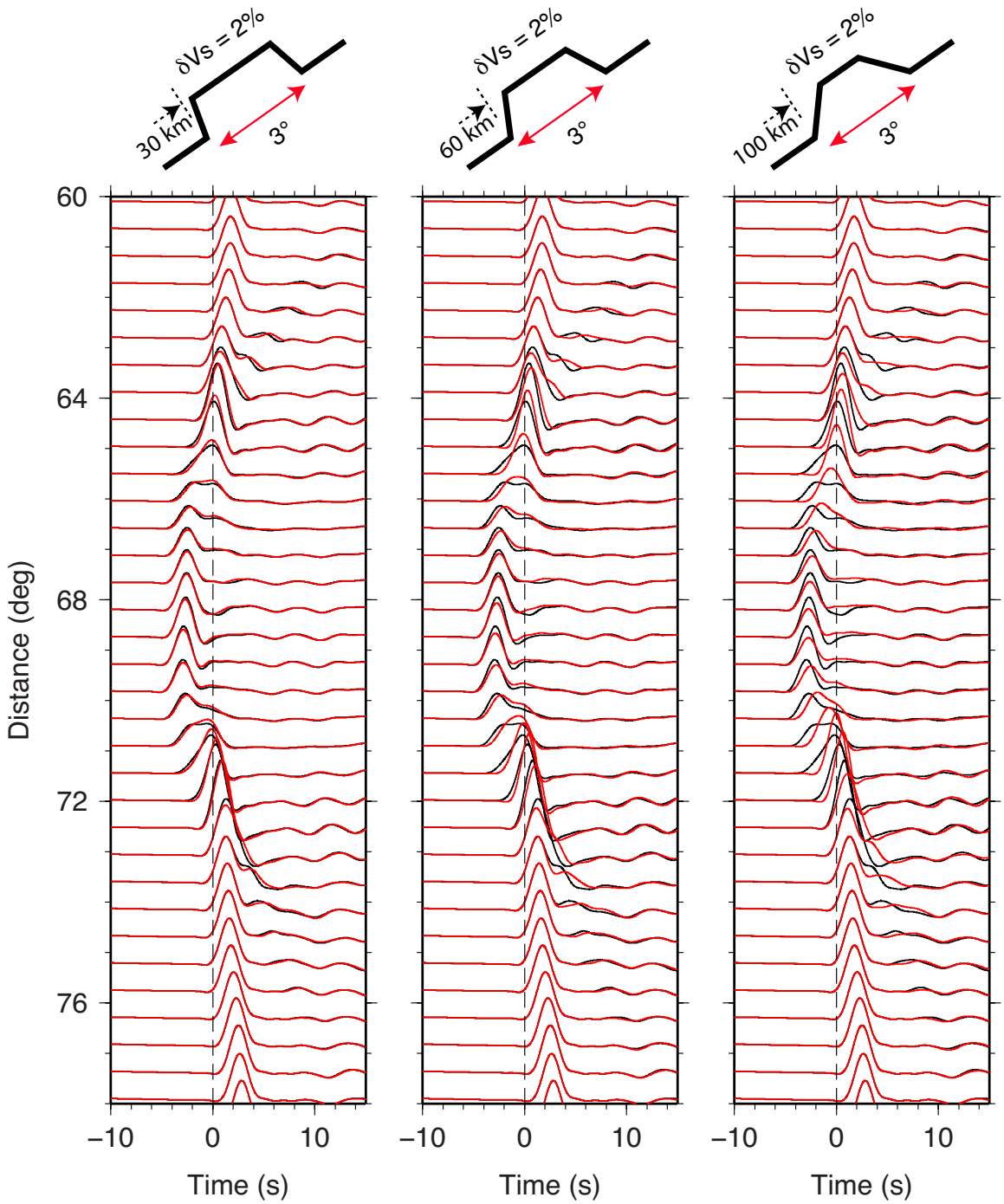

Figure S9. Predicted SH for slab models with different velocity gradient across the slab boundary. Black traces are the synthetics for a slab model with abrupt velocity change, transition width of 0, across the slab boundary. Red traces are the synthetics for different transition widths (from left to right: 30 km, 60 km, and 100km).

.

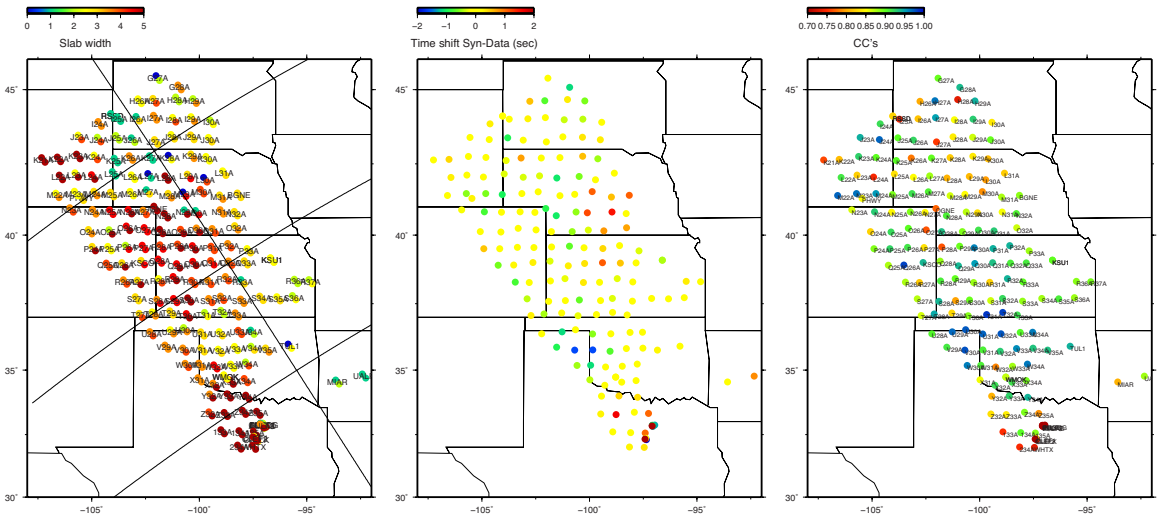

Figure S10. The inversion of slab thickness as presented in Fig. 9. From left to right: the inverted two thicknesses for each station plotted with two color circles next to the station; the time difference; and the cross-correlation coefficients between the simulated waveforms and the data.

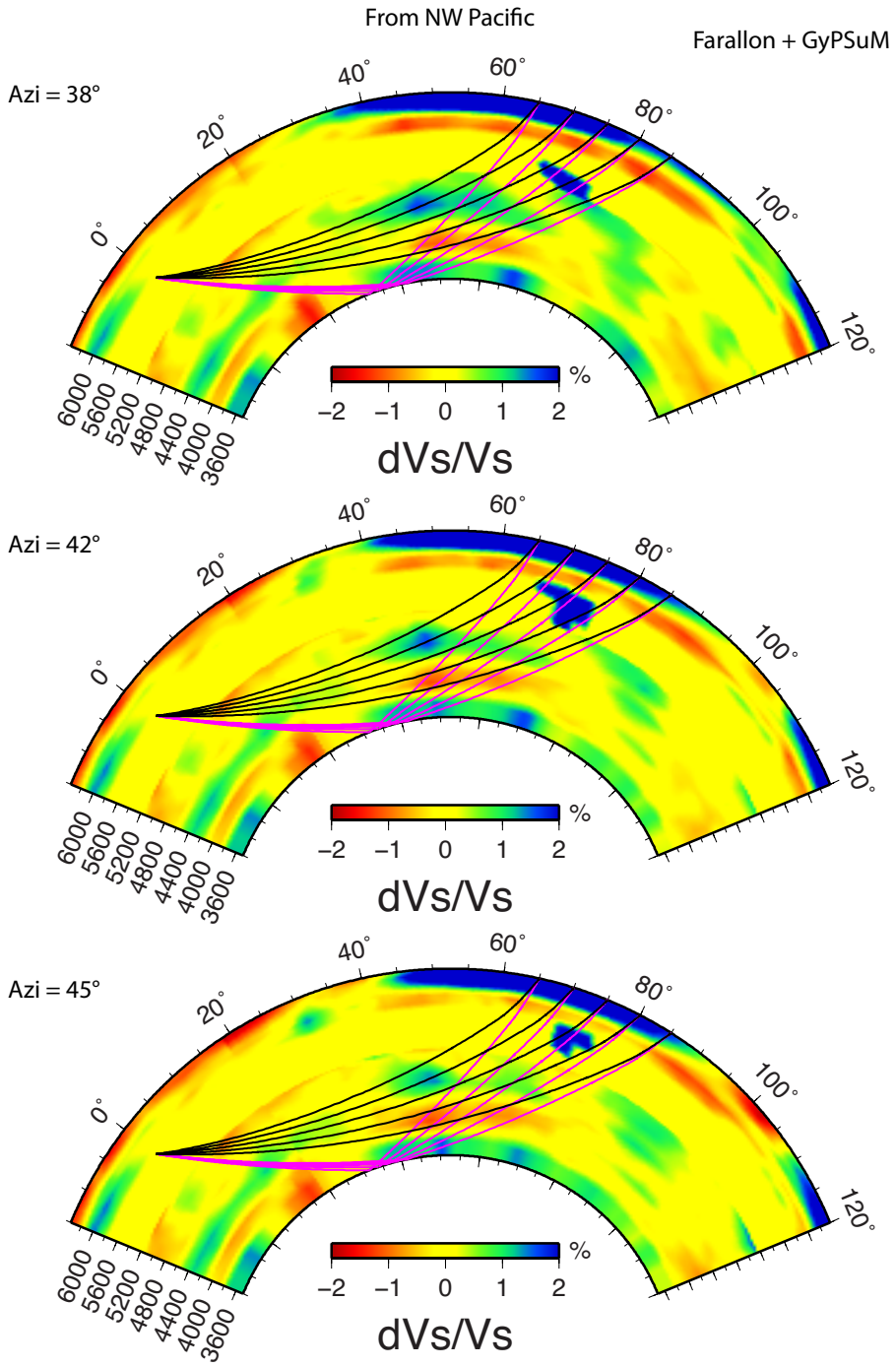

Figure S11. 2D cross section through the mega-slab model as in Fig. 11B along a great circle between an event at NW Pacific region and the USArray.

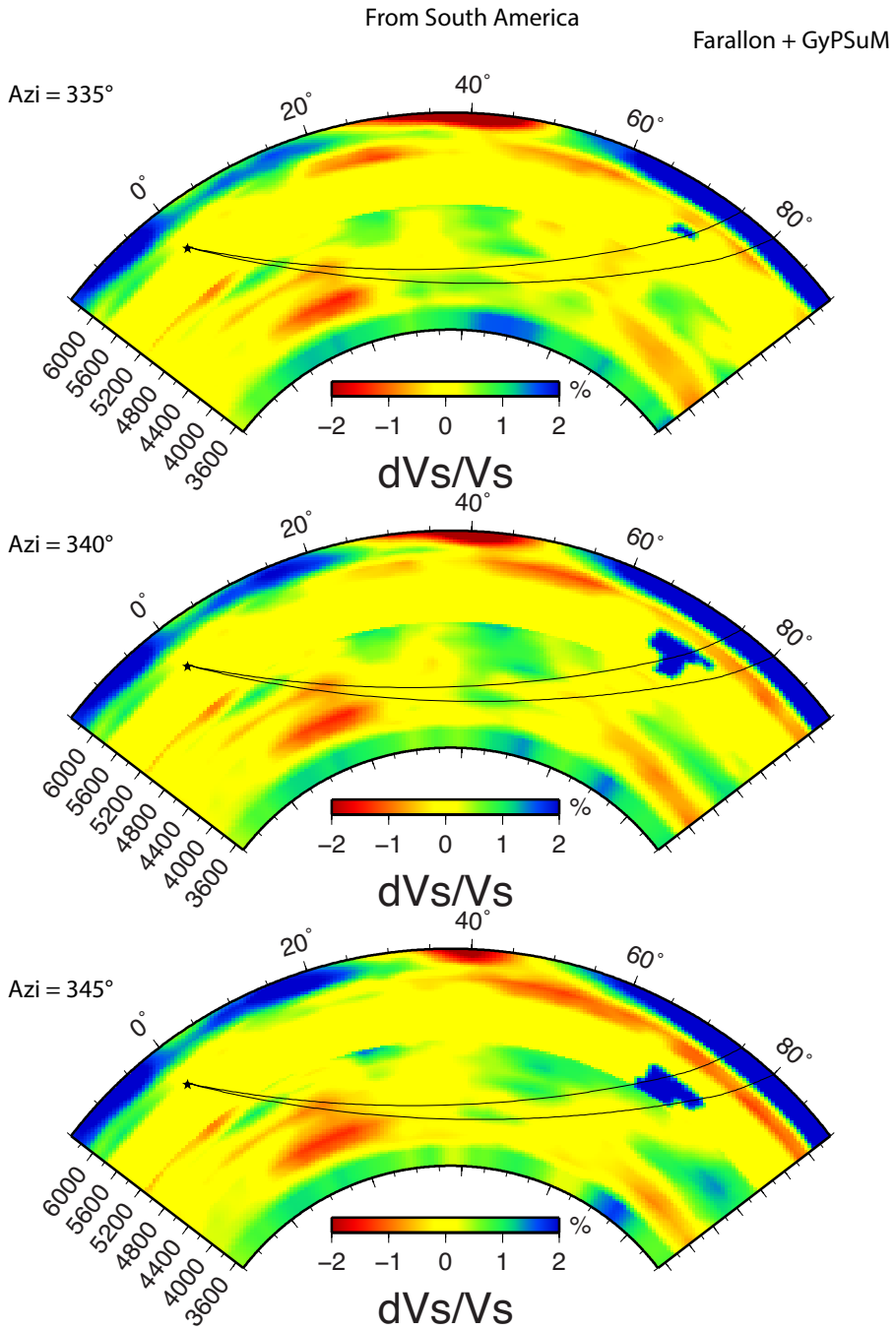

Figure S12. 2D cross section through the mega-slab model as in Fig. 11B along a great circle between an event at South America and the USArray.

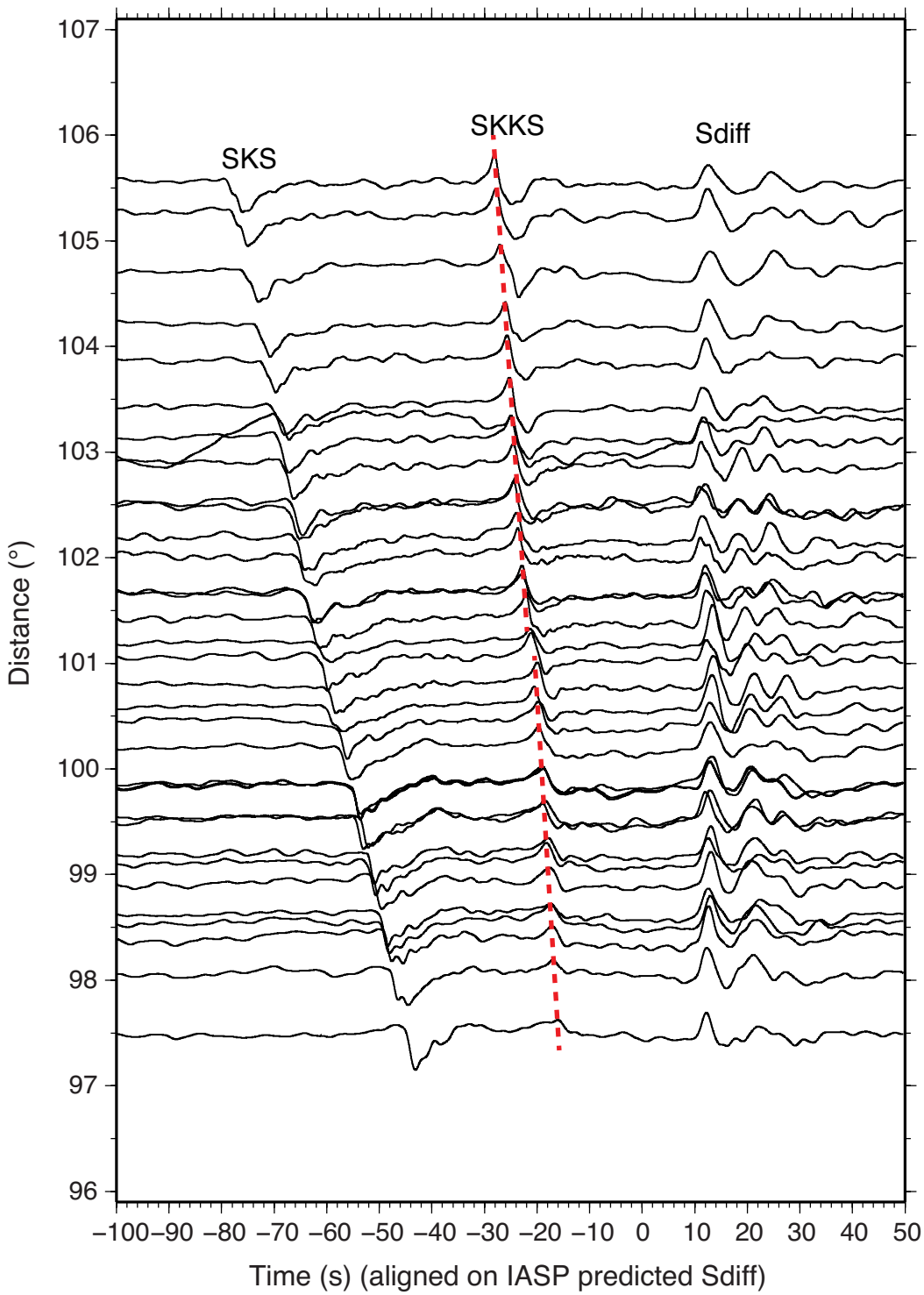

Figure S13. An example section of the SV data for the Fiji event 20110729 as in Fig. 11. The azimuth range is between 50° to 52°. The traces are aligned on the ISAP predicated S_{diff} travel time. Note all S_{diff}, SKKS, and SKS have faster arrivals crossing the distance of 101°.

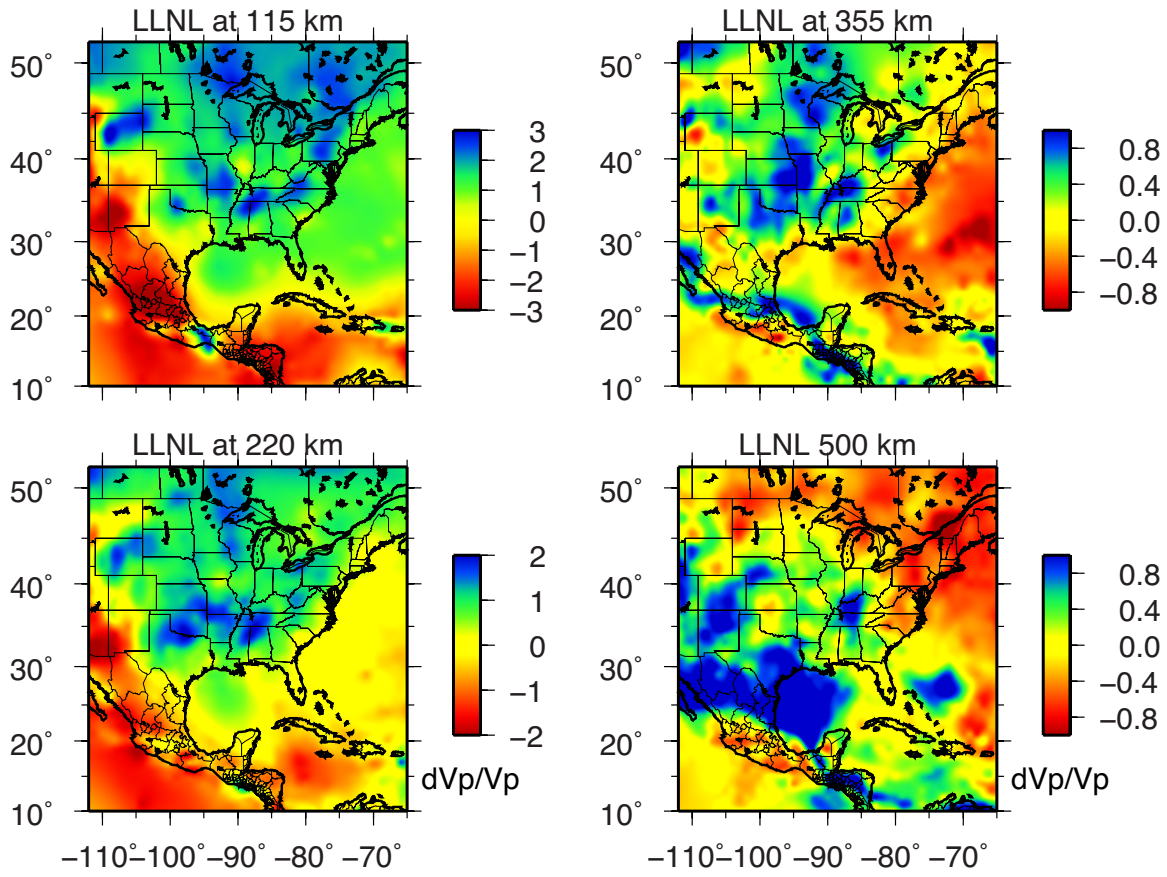

Figure S14. LLNL-G3Dv3 model at the depth of 115 km, 220 km, 355 km, and 500 km.

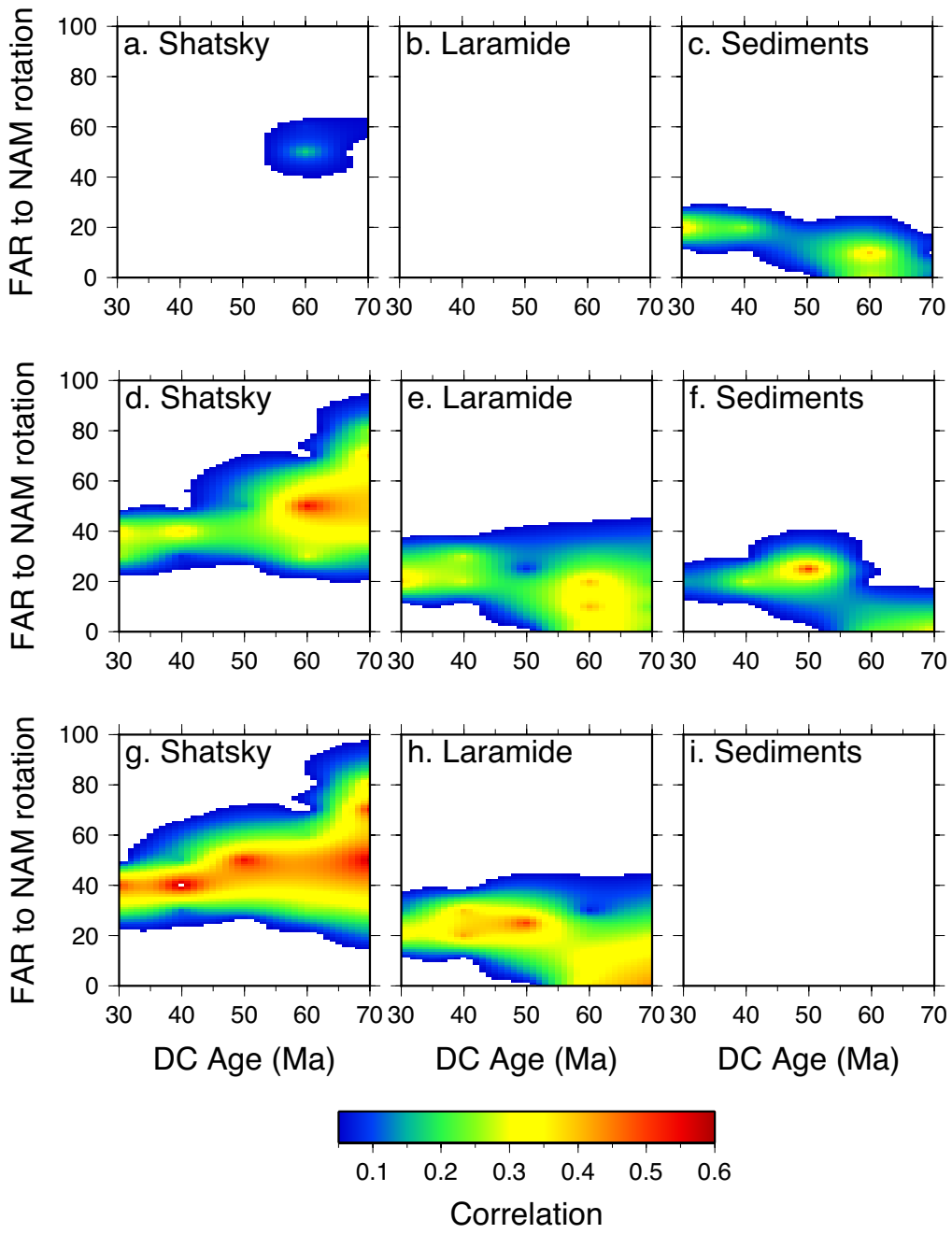

Figure S15. Correlation between the face of the slab that points upward and eastward and the Shatsky conjugate at 85 Ma, Laramide deformation 85-75 Ma, and sediment depocenter at 80-75 Ma. (a-c) is for the northern part, (d-f) the middle and (g-i) the southern part. A blank frame implies no correlation.

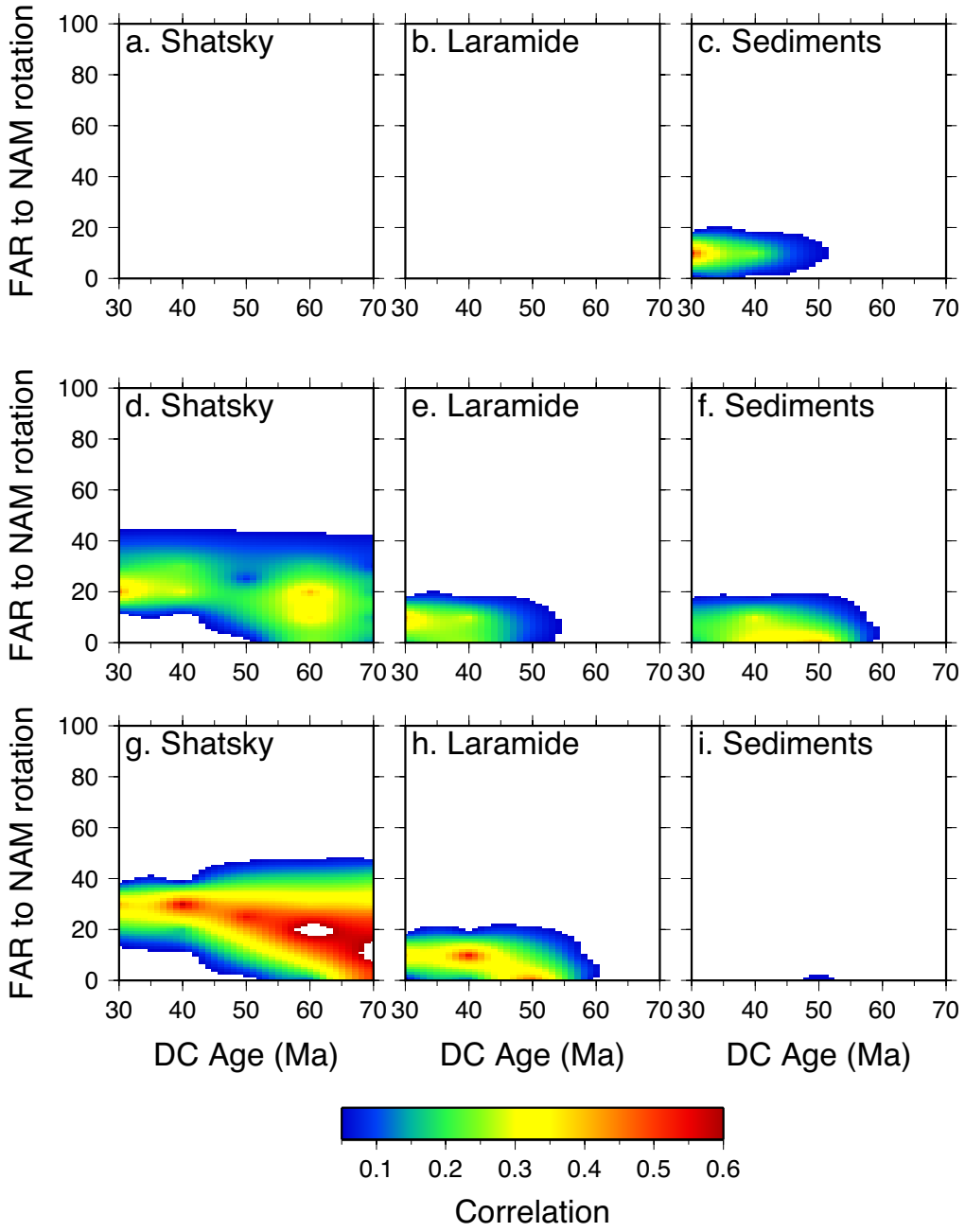

Figure S16. Correlation between the face of the slab that intersect at 660 km depth and the Shatsky conjugate at 85 Ma, Laramide deformation 85-75 Ma, and sediment depocenter at 80-75 Ma. (a-c) is for the northern part, (d-f) the middle and (g-i) the southern part. A blank frame implies no correlation.

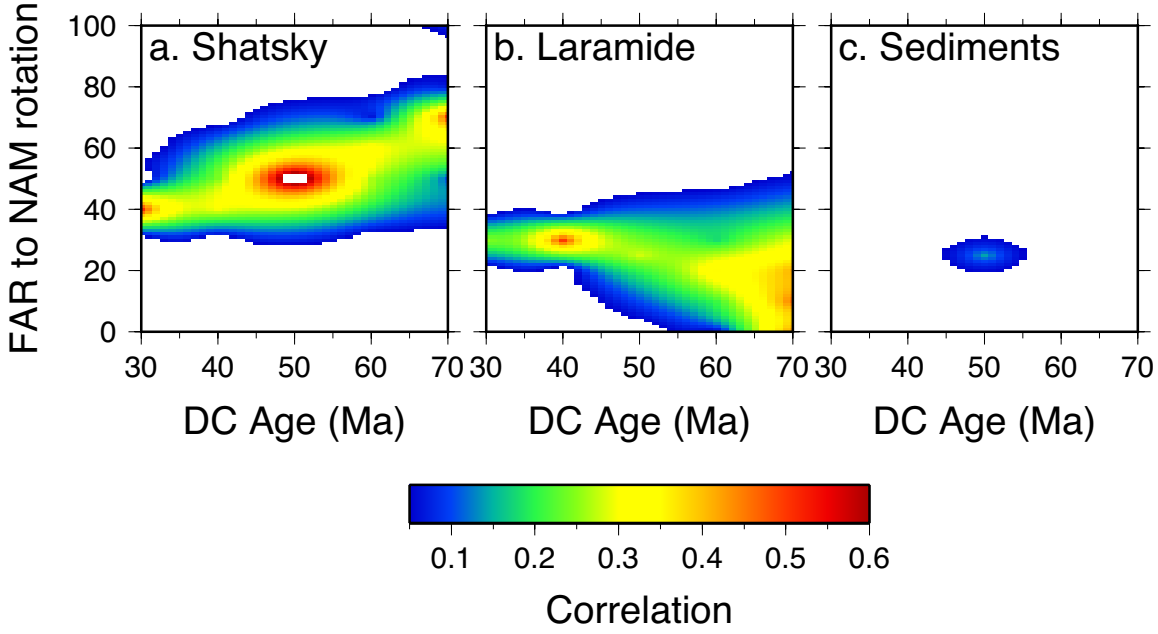

Figure S17. Correlation between the overlap of the middle mantle slab in TX2000 model [*Grand et al.*, 2002] (Fig. 3a) and the Shatsky conjugate at 85 Ma, Laramide deformation 85-75 Ma, and sediment depocenter at 80-75 Ma.